Type of the Paper (Article)

Extracting the Resistive Current Component from a Surge Arrester`s Leakage Current without Voltage Reference

Vid Vončina [1,*], Jože Pihler [2] and Miro Milanovic [2]

[1] Izoelektro d. o. o., Limbuš, 2341 Slovenia (e-mail: vid@izoelektro.si)
[2] University of Maribor Faculty of Electrical Engineering and Computer Science, 2000 Maribor, Slovenia, (e-mail: joze.pihler@um.si and e-mail: miro.milanovic@um.si).
* Correspondence: vid@izoelektro.si; Tel.: (optional; include country code; if there are multiple corresponding authors, add author initials) +xx-xxxx-xxx-xxxx (F.L.)

Abstract: This article presents the development of the theoretical background and the design of an electronic device for monitoring the condition of a gapless Metal Oxide Surge Arrester (MOSA). The device is intended to be used online. Due to the inaccessibility and possible remote location of most surge arresters, it is equipped with a communication system, allowing the device to convey the measurement of the surge arrester characteristics under any conditions. By gathering measurements of the surge arrester's resistive component of leakage current, it is possible to determine the condition of the MOSA. After interpreting the results, these can be sent via a data transfer unit to a server, which, in turn, sends it onward to the authorised personnel through the surge arrester control centre.

Keywords: IoT, leakage current, Metal Oxide Surge Arrester, remote monitoring, resistive component of leakage current.

---

1. Introduction

Crucial components in the transmission and distribution networks are protected against overvoltage by MOSA. For this reason, it is always of high importance to monitor their condition continuously. According to recent trends, monitoring is the most reliable way to decrease network losses and increase the reliability of equipment. The main components of MOSA are zinc oxide varistors (ZnO varistors), which are semiconductors that have a non-linear characteristic. This characteristic allows the MOSA to perform its function.

There are a few proposed methods that explain the conduction mechanism of the ZnO varistors. All of these consider the time and exposure of the MOSA to the overvoltage, so that the characteristic degrades to the point where the MOSA does not perform its function sufficiently, and, later, does not perform its function at all. Matsuoka [1], proposed the conduction method analysis based on the theory of Space Charge Limited Current (SCLC), Levinson and Philipp [2] explained the conduction mechanism by studying of the semiconductor tunnelling effects through a thin layer at the grain boundaries. Also, the tunnelling effect is the main topic in [3-10], where the authors put great emphasis on the behaviour of tunnelling effects on the Schottky barriers of the chosen semiconductors. The authors in [11-13] describe conduction phenomena by bypassing the effects in heterojunctions and induced holes during the breakdown in semiconductors. Also, the role of space charge in the electrical conduction processes for heterojunctions composed of thin films of ZnO and Bi2O3 is well described in [14].

The frequent and high overvoltages, moisture in the housing of the MOSA, overheating etc... are important factors that reduce the reliability of the MOSA. Overvoltage phenomena can be classified in to two groups, as:

- Atmospheric discharges;
- Consequences of switch devices` manipulations;

both of which have a destructive effect on the elements of the power system and reduce the reliability of their operation. Therefore, the important role of MOSA is to start operating immediately when an overvoltage occurs, and secondly, not to cause losses within the network due to excessive leakage current at continuous operation of electrical devices.

A few methods exist in order to determine the MOSA condition. These have been distinguished between online and offline methods. Popular are online testing methods, which range from fault indicators, disconnectors and surge counters to more sophisticated methods such as U-I characteristic curve analysis [15], the power loss method [16], leakage current measurements [17-21], temperature measurements [22-24], electro-magnetic field measurements [25], [26], etc. An example of such a method is also the Capacitive Current Compensation Method (CCCM), explained in [18], [19] and [27], which compensates the capacitive component to extract the resistive component I_r. However, the researchers in the area also paid significant attention to evaluating the surge arrester's condition to reduce network losses. According to the IEC 60099-5:2013, 2013 [28] an arrester is considered faulty at I_r=0.6 mA. If the arresters exceed this value and are not replaced, these produce additional power losses, financial losses and carbon footprint, as shown in Table 1, which are explained in the study performed in [29].

Table 1. Annual losses due to faulty surge arresters in (the Slovenian) distribution network.

	Annual for 1 MOSA	Annual for 12,090 pcs of MOSA
Power losses [MWh]	0,486	5,872
Financial losses [€]	35,4	428,312
Carbon footprint [t]	0,133	16,4416

The offline methods are performed in laboratories and are more expensive, due purely to the manipulation involved in dismantling and transporting of the MOSA to an adequate facility where all the tests can be performed or supplied with an independent voltage source for testing. Such a method is the Point On Wave Method (POWM) described in [30], which is more convenient for use because it does not require measurement of the voltage. Another popular offline method is where only the fundamental component of the capacitive current is subtracted. The Resistive Current Wave shape-based Method (RCWM) [15] results in the harmonic content of the capacitive component being added to the resistive component.

This paper deals with the developing of the principle and electronic device capable of a real-time arrester monitoring operation. Section 2 describes the physical background for the arrester condition monitoring principle, based on the leakage current measurement and analogue and digital acquisition of the collected measurement data. Based on the theoretical conclusion, the measurement device is designed, and described in Section 3. It consists of three main parts, the analogue and digital signal acquisition and communication units. Section 4 deals with experimental verification of the algorithm and electronic device.

2. Physical Background of the Arrester Monitoring Principle

The functionality of the arrester monitoring system is based on the physical background of the leakage current study. From the measured leakage current (I_t), it is necessary to extract the resistive component (I_r). During long-time operation the arresters encounter thermal stresses, due to the power losses caused by leakage current. The power dissipation can be calculated as follows:

$$P_d = \frac{W}{T} = \frac{1}{T}\int_0^T U(\omega t) I_t(\omega t)\, d\omega t \,, \tag{1}$$

where P_d represents the average power-dissipation, W represents the energy, T is the period of voltage $U(\omega t)$ which causes the current $I_t(\omega t)$, and ω represents the angular frequency. The current through a brand-new arrester is relatively small (the order of a few 10 μA), but, due to high voltage, the dissipation becomes significant as the arrester deteriorates. It is also known that the voltage is contaminated by high order harmonics[i], mainly with the 3rd and 5th harmonic components, so, the voltage and current in (1) can be described as the sum of higher harmonic components as follows:

$$U\left(\omega t\right)=\sum_{n=1}^{\infty}\hat{U}_n\sin\left(n\omega t\right), \tag{2}$$

$$I_t\left(\omega t\right)=\sum_{n=1}^{\infty}\hat{I}_{t,n}\sin\left(n\omega t\right), \tag{3}$$

where $\hat{U}_n$ and $\hat{I}_{tn}$ represent the magnitudes of the n^{th} voltage and current harmonic components, respectively. After substitution of (2) and (3) into (1), and after a short manipulation, the equation is as follows:

$$\begin{aligned} P_d &= \frac{\hat{U}_1\hat{I}_{t,1}}{2}\cos\Phi+3\frac{\hat{U}_3\hat{I}_{t,3}}{2}\cos3\Phi+5\frac{\hat{U}_5\hat{I}_{t,5}}{2}\cos5\Phi+\cdots n\frac{\hat{U}_n\hat{I}_{t,n}}{2}\cos\left(n\Phi\right) \\ &= U_1I_{t,1}\cos\Phi+3U_3I_{t,3}\cos3\Phi+5U_5I_{t,5}\cos5\Phi+\cdots nU_nI_{t,n}\cos\left(n\Phi\right), \end{aligned} \tag{4}$$

where $U_n=\hat{U}_n\big/\sqrt{2}$ and $I_{t,n}=\hat{I}_{t,n}\big/\sqrt{2}$; $n=1,3,5,\ldots$ represent the root mean square (rms) values of the voltages and currents, respectively, and Φ is the phase delay between current and voltage. The current resistive component represents the measure of the arrester's quality, when $I_{r,rms}$ exceeds the value defined by the Standard [28] $\left(I_{r,rms}>600\big/\sqrt{2}\ \ \mu\text{A}\right)$ the arrester is in bad condition, and should be replaced by a new one. A few different MOSA (ten samples) with a nominal voltage of 36 $[\text{kV}]_{\text{rms}}$ have been chosen randomly for measurements in order to design in advance, so-called "static characteristics". By presuming that the arresters are made from the same materials under the same production conditions and connected to the same supply voltage U, it is expected that they have statistically similar static characteristics as:

$$\hat{I}_r=\hat{I}_r\left(\varphi\right), \tag{5}$$

The measurement principle is based on the classical off-line measurement procedure suggested in [28]. The magnitude of the resistive current component ($\hat{I}_r$) is extracted from the oscillograms at the instant when the voltage is at its peak (dU/dt=0), as shown in Figure 1 (a). Figure 1 (b) shows the phasor diagram at ωt=φ of leakage current I_t, and its resistive and capacitive components I_r and I_c, respectively. The harmonic distortion obtained as a projection of the phasor I_t to the real (Re) axis causes that distortion of the resistive current is acceptable, and the magnitude $\hat{I}_r$ is accurate enough for further analyses. However, at the same time when $\hat{I}_r$ is extracted from the diagram, the grey shaded areas indicated in Figure 1 (a) and (c) as I_{t_avg} are extracted as well, and it depends on φ and $\hat{I}_r$ as follows:

$$I_{t\_avg}=I_{t\_avg}\left(\varphi,\ \hat{I}_r\right) \tag{6}$$

and it represents an average value of the current I_t, in the chosen interval (for example $\pi/3\le\omega t\le\pi$) as follows:

$$I_{t\_avg}=\frac{3}{2\pi}\int_{\pi/3}^{\pi}I_t\left(\omega t\right)d\omega t\,. \tag{7}$$

---

[i] The voltage in the observed power system is contaminated with a third harmonic U_3=0.1 % of U_1, fifth harmonic U_5=0.3 % of U_1 and e.c.t.

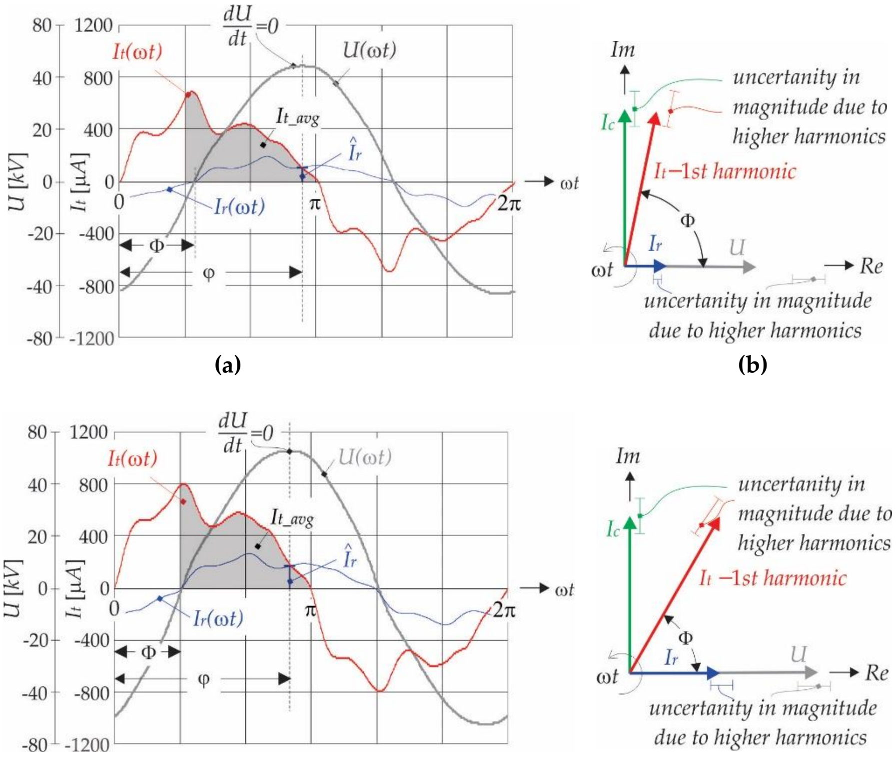
(a) (b)

(c) (d)

Figure 1. (a) Current and voltage wave shape when U=27 [kV]$_{rms}$; (b) Phasor diagram, when Φ=72°; (c) Current and voltage wave shape when U=37 [kV]$_{rms}$; (d) Phasor diagram, when Φ=64 °.

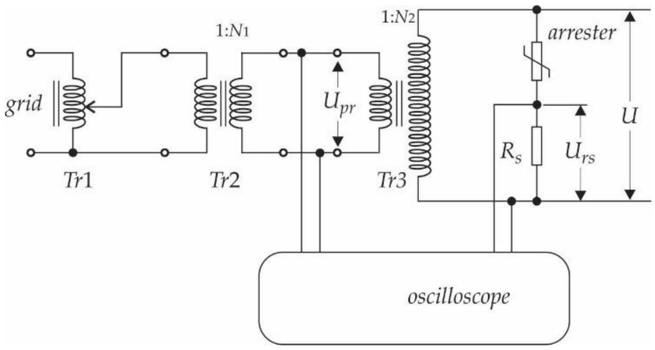

Figure 2. Measurement set-up scheme.

2.1. Extraction of the resistive current magnitudes from the arrester's leakage current

To extract the resistive current component $(\hat{I}_r)$ from the leakage current (I_t) the measurement is performed at a few different operating points (different supply voltages U). The measurement set-up[ii] is organised as presented in Figure 2. Figures 3 (a)-(f) show measurement results obtained from CSV data (from an oscilloscope), of randomly chosen arrester[iii]. The magnitude of the resistive current component ($\hat{I}_r$) is extracted from the oscillograms at the instant when the voltage is at its peak (dU/dt=0) at six operating points. Further, the measurements were performed on 10 arresters in order to have a representative result. Table 3 shows the obtained measurement results. For every sample, the exact value of the phase angles (φ) and the magnitudes of $\hat{I}_r$, are indicated for every operating point.

[ii] The following equipment was used in the set-up: A $Tr1$-autotransformer up to 0.4 [kV], a $Tr2$-transformer for galvanic isolation 1/N_1=0,4/7 [kV], a high voltage transformer, 1/N_2=0.1/110 [kV], an oscilloscope RIGOL DS4034, multimeter Fluke 189.

[iii] Arrester type SNO_U=36 kV class DH producer IZOELEKTRO.

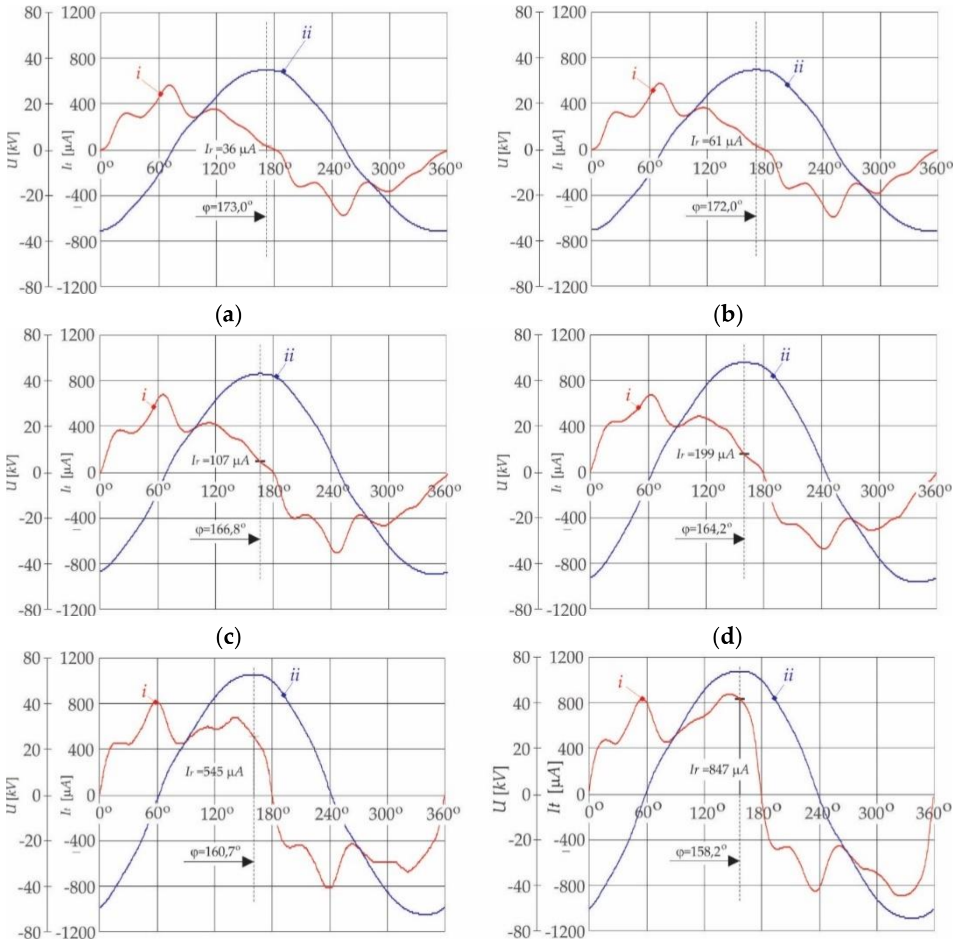

(**a**) (**b**)

(**c**) (**d**)

(**e**) (**f**)

Figure 3. Measured current (I_t) and voltage (U) with oscilloscope (CSV files) I_t: ***i*** arrester leakage current; ***ii*** measured arrester voltage (U): (**a**) at U=25 kV$_{\mathrm{rms}}$, φ=173.0°, $\hat{I}_r$=61 µA; (**b**) at U=27 kV$_{\mathrm{rms}}$, φ=172.0°, $\hat{I}_r$=61 µA; (**c**) at U=31 kV$_{\mathrm{rms}}$, φ=166.8°, $\hat{I}_r$=107 µA; (**d**) at U=36 kV$_{\mathrm{rms}}$, φ=164.2°, $\hat{I}_r$=199 µA; (**e**) at U=37 kV$_{\mathrm{rms}}$, φ=160.7°, $\hat{I}_r$=545 µA; (**f**) at U=39 kV$_{\mathrm{rms}}$, φ=158.2°, $\hat{I}_r$=847 µA.

Table 3. Resume of measured phase delay φ and resistive component $\hat{I}_r$ extracted from the oscilloscope.

sample 1		*sample 2*		*sample 3*		*sample 4*		…	*sample N*		*mean val.*			*Relative σ*	
φ_1 [°]	$\hat{I}_{r,1}$ [µA]	φ_2 [°]	$\hat{I}_{r,2}$ [µA]	φ_3 [°]	$\hat{I}_{r,3}$ [µA]	φ_4 [°]	$\hat{I}_{r,4}$ [µA]	….	φ_N [°]	$\hat{I}_{r,N}$ [µA]	φ [°]	$\hat{I}_r$ [µA]	U_{rms} [kV]	σ_φ [%]	$\sigma_{\hat{I}_r}$ [%]
157	812	158	847	158	847	155	755	….	156	750	157	802	39	0.31	3.9
159	510	160	521	161	545	160	475	….	159	480	160	500	37	0.36	4.3
162	220	163	214	165	199	162	195	….	163	183	163	202	36	0.59	7.3
165	107	166	102	167	107	164	95	….	166	102	166	103	33	0.67	4.8
168	66	169	56	169	61	171	56	….	171	60	170	59	31	0.88	5.8
173	33	172	33	173	36	174	36	….	173	37	173	35	25	0.39	5,5

From Table 3 it is evident that there are a few measurement results showing every arrester pair φ and $\hat{I}_r$. From these values it is convenient to calculate the average values, which usually represent the most probable value. So, the statistical parameters, as average values for phase delay (φ) are:

$$\varphi = \frac{1}{N}\sum_{k=1}^{N}\varphi_k \ , \tag{8}$$

the average values of resistive current magnitudes ($\hat{I}_r$),

$$\hat{I}_r = \frac{1}{N}\sum_{k=1}^{N}\hat{I}_{r,k} \ , \tag{9}$$

the other statistical parameters such as the relative Standard Deviation of phase delay (σ_φ) and of current magnitudes ($\sigma_{\hat{I}_r}$)

$$\sigma_\varphi = \frac{1}{\varphi}\sqrt{\frac{\sum_k^N(\varphi_k-\varphi)^2}{N-1}} \ , \tag{10}$$

$$\sigma_{\hat{I}r} = \frac{100}{\hat{I}_r}\sqrt{\frac{\sum_k^N\left(\hat{I}_{r,k}-\hat{I}_r\right)^2}{N-1}} \ , \tag{11}$$

are calculated for the same operation points and are indicated in Table 3 (grey shaded columns). The numbers extracted from the waveforms in Figures 3 (a)-(f) are indicated in Table 3 as *sample* 3 results.

2.3. Description of the measurement principle for the average value of leakage current at certain intervals

As can be concluded from the above description, such measurement of leakage current can only be performed off-line. This method is not appropriate for real-time measurement, with the requirements that the voltage *U* should not be measured because of safety reasons of the whole system. When only leakage current is measured, there is no information about phase delay. But it can be noticed, as shown in Figure 4, that the magnitude $\hat{I}r$ corresponds with exactly one average value of I_t evaluated in the interval $\pi/3 \le \omega t \le \pi$. This interval can be chosen arbitrarily; in this case it was chosen that the third harmonic component has no influence on average value. So, the average value I_{t_avg}, for the real-time measurement can be evaluated as follows:

$$I_{t\_avg} = \frac{3}{2\pi}\int_{\pi/3}^{\pi} I_t(\omega t)\, d\omega t = \frac{1}{n-k}\sum_{m=k}^{m=k+n} I_{t(m)} \ , \tag{12}$$

where *k* is the starting point index and *n* is the end-point index of current instants (Figures 4). The average values (I_{t_avg}) were calculated for different arresters at different operating points, and are collected in Table 4. The statistical parameters, the average phase delay φ, are calculated by (8), and the mean value $I_{t,mn}$, which corresponds with the phase delay, is calculated as follows:

$$I_{t,mn} = \frac{1}{N}\sum_{k=1}^{N} I_{t\_avg,k} \ , \tag{13}$$

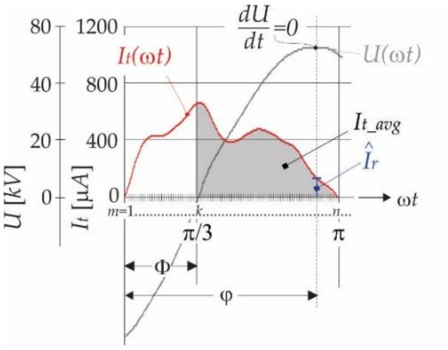

Figure 4. Description of average value I_{t_avg} and its relation with pair $\left(\varphi,\ \hat{I}_r\right)$.

Table 4. Resume of calculated average value of leakage current I_t, measured with an oscilloscope in the interval $60^0 \le \varphi \le 180^0$ $(\pi/3 \le \omega t \le \pi)$, according to the relation $I_{t\_avg} = I_{t\_avg}(\varphi)$

sample 1		*sample 2*		*sample 3*		*sample 4*			*sample N*		*mean val.*			*Relative σ*	
φ [°]	$I_{t\_avg,1}$ [μA]	φ [°]	$I_{t\_avg,2}$ [μA]	φ [°]	$I_{t\_avg,3}$ [μA]	φ [°]	$I_{t\_avg,4}$ [μA]	…	φ [°]	$I_{t\_avg,N}$ [μA]	φ [°]	$I_{t,mn}$ [μA]	U_{rms} [kV]	σ_φ [%]	$\sigma_{It,mn}$ [%]
157	643	158	665	158	664	155	621	…	156	640	157	646	39	0.73	2.5
159	546	160	548	161	545	160	523	…	159	522	160	537	37	0.43	2.2
162	426	163	420	165	418	162	380	…	163	401	163	409	35	0.68	4.1
165	359	166	353	167	356	164	340	…	166	365	166	355	33	0.46	2.4
168	329	169	319	169	318	171	314	…	171	321	170	320	31	0.72	1.5
173	298	172	294	173	301	174	305	…	173	310	173	299	25	0.27	2.0

and shown in Table 4 (grey shaded columns). Also, the relative Standard Deviation for the average of $I_{t,mn}$ at certain interval ($\sigma_{It,mn}$), are calculated at the same operation points as:

$$\sigma_{It,mn} = \frac{100}{I_{t,mn}} \sqrt{\frac{\sum_k^N \left(I_{t\_avg,k} - I_{t,mn}\right)^2}{N-1}}, \tag{14}$$

and are shown in Table 4. Based on the results in Tables 3 and 4, the so-called "static" characteristics are drawn to obtain analytical expressions. The obtained curves shown in Figure 5 can be approximated by sectional linear function. Because $I_{t,mn}(\varphi)$ is the consequence of , $\hat{I}_r(\varphi)$ the intersection of the linear function appears at the same argument, when $\varphi = \varphi_i$ [iv]. So, the trend lines, represented by the linear function are:

- when $60^o < \varphi \le \varphi_i$;

$$\hat{I}_r(\varphi) = -95.7\varphi + 15793 \tag{15}$$

$$I_{t,mn}(\varphi) = -38.1\varphi + 6615.6 \tag{16}$$

- when $\varphi_i < \varphi \le 180^o$;

$$\hat{I}_r(\varphi) = -9.03\varphi + 1593.7 \tag{17}$$

$$I_{t,mn}(\varphi) = -7.56\varphi + 1603.9 \tag{18}$$

Both characteristics, for certain arrester types, must be measured in advance, and prepared for further customer application (for example, these must be available in the arrester's data sheet).

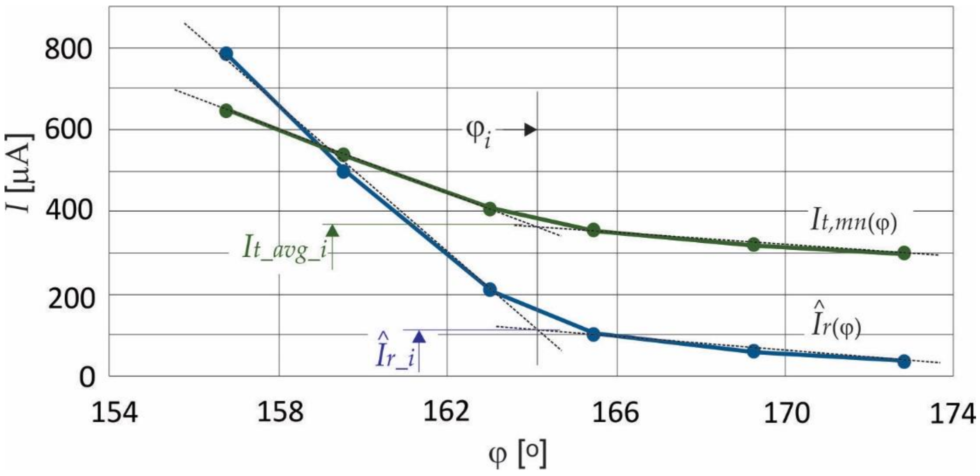

Figure 5. Static characteristics of $\hat{I}_r = \hat{I}_r(\varphi)$ and $I_{t,mn} = I_{t,mn}(\varphi)$

[iv] Calculating intersection of (15) and (17) gives $\varphi_i = 164{,}2^o$, $I_{t,mn,i} = 363\ \mu A$

2.3. Verification of the proposed algorithm

The algorithm is verified considering (15) to (18) after measuring of the unknown arrester, but extracted from the set of the same type. The arrester leakage current is sampled in the range $\varphi \in (60,\ 180)$ [°] and the value of I_{t_avg} is obtained. The proposed algorithm is shown in Figure 6 as a UML diagram.

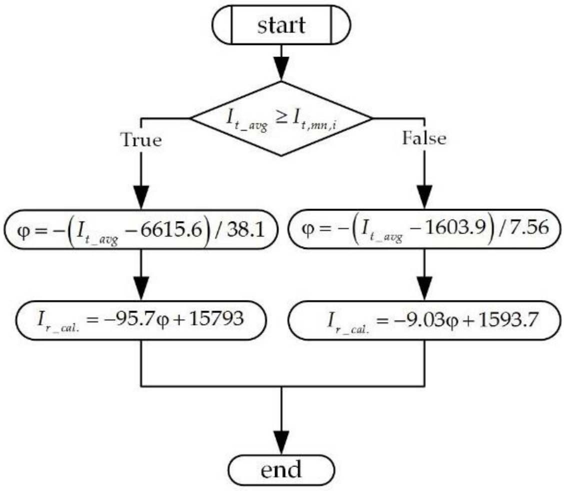

Figure 6. UML diagram for the functional mapping algorithm, $I_{t\_avg} \rightarrow \varphi \rightarrow \hat{I}_{r\_cal.}$

The obtained results are shown in Table 5. Current, indicated by $I_{r\_cal.}$, is obtained by using the formulas according to the block diagrams shown in Figure. 6.

Table 5. Verification of measurement results

Measured values	*Phase*	*Calculated* (15)-(18)	*Scope value*	*Relative error*
I_{t_avg}[µA]	φ[°]	$\hat{I}_{r\_cal.}$ [µA]	$\hat{I}_r$ [µA]	ε [%]
665	156.25	839	847	0.9
643	156.86	783	812	3.6
522	160.01	480	480	0.0
418	162.74	218	199	-9.8
356	165.06	103	107	3.5
319	169.95	59	56	-5.4
298	172.72	34	33	-3.0
570	158.75	600		

The results in Table 5 were recalculated according to the randomly chosen data from Tables 3 and 4. In the first column are data from Table 4, the second and third columns present the recalculated phase delay and magnitudes of unknown resistive current $\hat{I}_{r\_cal.}$, and in the fourth column are the collected "oscilloscope" data from Table 3. The relative error is also calculated, and is always inside the interval $\varepsilon \in \left(-2\sigma_{\hat{I}r}, 2\sigma_{\hat{I}r}\right)$, defined by the relative Standard Deviation (Table 3). The predicted limit of resistive current component is shown in the last row in Table 5, which appears at $I_{t,mn}$=570 µA with the phase delay of φ=159°. So, every measured $I_{t,mn}$ above this number indicates that the arrester should be replaced with a new one.

3. Surge Arrester Monitoring Device (SAMD)

Analogue input devices, such as an Analogue-to-Digital Converter (ADC) in conjunction with a separate operational amplifier (op-amp), were used to convert a time-varying analogue signal (I_t) into digital representations for further analyses in the microcontroller or a personal computer (PC).

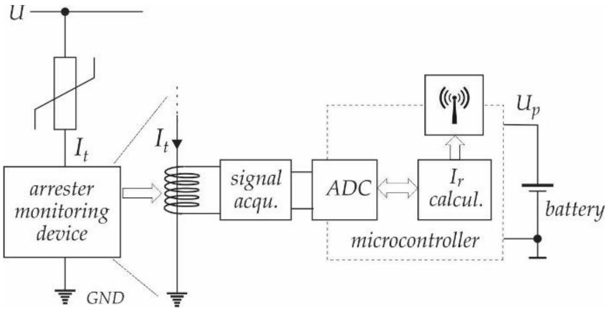

Figure 7. The block scheme of SAMD

Figure 7 shows the block scheme of the proposed electronic circuit. In order to obtain leakage current (I_t) values (samples) an ADC is used with an appropriate acquisition circuit. As a part of the conversion, the signal acquisition circuit is designed as an instrumentation amplifier. The key characteristics are high input impedance, high common-mode rejection, low output offset and low output impedance. After digitalisation of the leakage current (I_t), it is necessary to extract the resistive current component $\hat{I}_r$ using the algorithm based on the UML diagram shown in Figure 6. The resistive component can be calculated in the micro-controller, or digitalised leakage current can be sent through communication channels to the server, where the $\hat{I}_r$ can be calculated off line, but in "soft" real time.

Based on the above description, it can be summarised that the measurement device must fulfil the following requirements:

- Galvanic isolation of the measured signal (safety reason);
- Acquire and prepare the analogue signal for digital conversion;
- Collection of current samples in the range $\varphi \in (\varphi_{\min}, \varphi_{\max})$;
- Prepare information for Wi-Fi transfer to an off-line server.

3.1 Electronic Circuits

The analogue acquisition unit is organised as a transimpedance op-amp with appropriate gain and common mode rejection ratio. Such a process requires precise and stable measurement of "small" alternative current (measuring range $I_t \in (-3\text{ mA}, +3\text{ mA})$) when the op-amp is single voltage supplied ($U_p = 3\text{ V}$). The current I_t is captured by using an acurrent transformer with the appropriate ratio (1:300). Such a ratio is chosen as a compromise between the sensitivity to measurement of leakage current and rejection of the currents' strokes of a few hundreds of Ampere ($I_t : I_{t,stroke} = 1:10^7$). This is solved by using an appropriate protection of op-amp inputs. The battery voltage measurement and temperature measurement circuits are also integrated into the device.

3.1.1 Protection Circuit

The whole measurement circuit is protected over the current's strokes, and some high frequency interferences shall be rejected (common mode (CM) and differential mode (DM) interferences). Figure 8 shows the over-current protection performed using two Schottky and four Zener diodes. All diodes were chosen in order to keep the voltage difference smaller than the supply voltage (V_2-V_1<U_p).

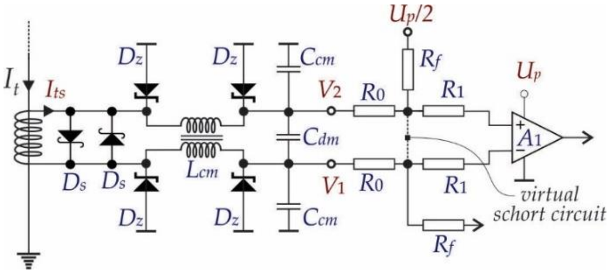

Figure 8. Protection and CM and DM noise reduction circuit

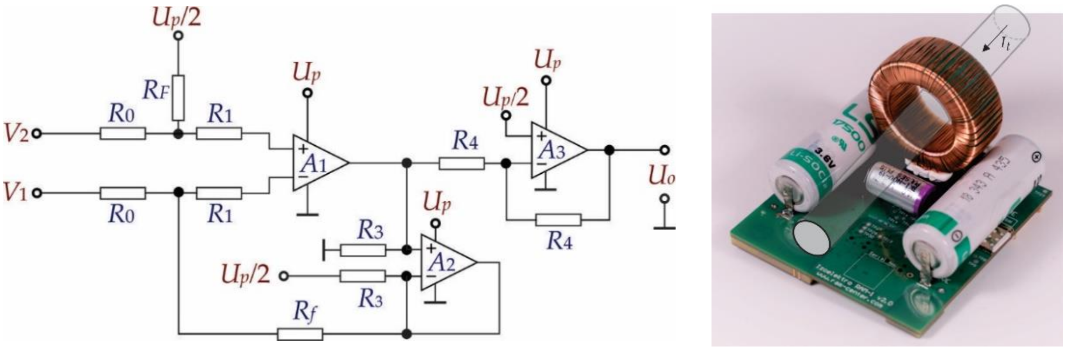

(**a**) (**b**)

Figure 9. (a) Analogue signal acquisition circuit; (b) PCB with components of the measurement device

The high frequency interferences (noises) were reduced by using an *LC* filter, which contains a Common Mode (*CM*) choke coil (L_{cm}), two line-bypass capacitors (C_{cm}) for suppressing the *CM* noise signals and an across-the-line capacitor (C_{dm}) for suppressing the Differential Mode (*DM*) noise signals.

3.1.2 Signal Acquisition Circuit

Hereinafter referred to as the circuit in Figure 8, the current transformer secondary current (I_{ts}) is converted to voltage difference on the resistances R_0. Due to the properties of the almost infinite open loop gain of the op-amp A_1 and the used feed-back by R_f, it follows that:

$$V_2 - V_1 = 2R_0 I_{ts}\,, \tag{19}$$

where R_0 indicates the resistances in the input loop of the operational amplifier A_1 and $I_{ts}=I_t/300$[v]. Also, the alternative input signal must be transformed into a unipolar signal appropriate for A-D conversion of voltage at the output of the measurement system (U_{oA3}). Figure 9 shows the scheme of the chosen electronic circuit. The frequency analyses of the electronic circuit were considered in order to design a suitable gain and band-pass. Assuming that the operational amplifiers are the same type, and after analyses of the scheme in Figure 9, it follows:

$$U_o = \frac{A_\beta\left(\beta_1 s + 1\right)}{\alpha_2 s^2 + \alpha_1 s + 1}\left(V_2 - V_1\right) + \frac{U_p}{2}\,, \tag{20}$$

where $A_\beta=R_f/R_0$ represents closed-loop gain, $\beta_1=1/\omega_t$, $\alpha_2=1/(B\omega_t^2)$, $\alpha_1=1/(B\omega_t)$, $B = R_0/(R_F + R_0)$[vi], ω_t is unity-gain bandwidth[vii] (usually specified on the data sheets of op. amps.), and U_p denotes the power supply voltage. Using (20) and considering that $s \to 0$, the output voltages can now be calculated as:

$$U_o = \frac{R_f}{R_0}\left(V_2 - V_1\right) + \frac{U_p}{2}\,, \tag{21}$$

---

[v] $V_2 - V_1 = 2R_0 I_{ts} \Rightarrow V_2 - V_1 = 0.47$ mV

[vi] $R_0 = 47\ \Omega,\ R_F = 100\ \mathrm{k\Omega}$

[vii] $\omega_t = 2\pi f \ \Rightarrow\ \omega_t = 2\pi 4\times 10^5\ rad/s$ (from the data sheet)

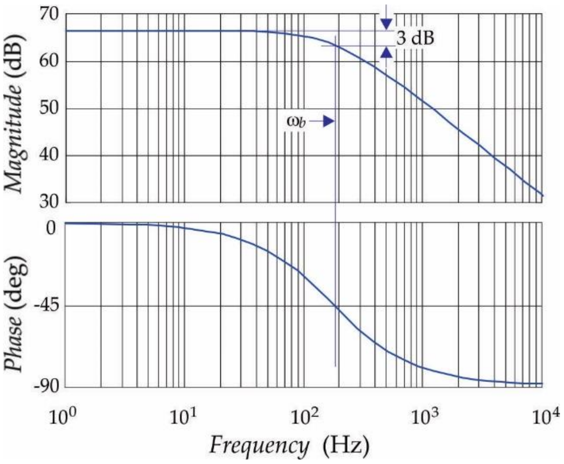

Figure 10. Bode diagram of $H_o(s)$

Based on (21) the output voltage range of the chosen instrumental amplifier gain can be defined for the whole range of the leakage current[viii]. Also, based on (20), the transfer function for alternative difference signal was considered when DC offset ($U_p/2=0$) was excluded, as follows:

$$H_0(s) = \frac{U_o(s)}{V_2(s)-V_1(s)} = \frac{A_\beta(\beta_1 s+1)}{\alpha_2 s^2+\alpha_1 s+1} \Rightarrow H_0(s) \approx \frac{A_\beta}{1+\dfrac{s}{\omega_b}}, \tag{22}$$

where ω_b represents the small-signal bandwidth frequency[ix] which can be obtained after the short calculation:

$$\omega_b = \frac{\omega_t}{\left(1+\dfrac{R_f}{R_0}\right)} \Rightarrow f_b = \frac{f_t}{\left(1+\dfrac{R_f}{R_0}\right)}, \tag{23}$$

For certain data parameters and using MATLAB, the frequency characteristics are calculated, and shown in Figure 10.

Unfortunately, the op-amp devices consist of non-ideal components which can introduce some deviation into the measurement results. The sensitivities function S_x^y can be used in order to quantify this inconsistence. This function is defined as:

$$S_x^y = \frac{\partial y}{\partial x}\frac{x}{y}, \tag{24}$$

where x denotes the variable of interest. According to (22), a closed-loop gain A_β, a frequency ω_b and y denote the circuit parameters, as is the absolute form of the function $H(j\omega)$ as follows:

$$H_\beta = \left|H(j\omega)\right| = \frac{A_\beta}{\sqrt{1+\left(\dfrac{\omega}{\omega_b}\right)^2}}, \tag{25}$$

Using (24) and according to the variables of interest, two sensitivities ($S_{A_\beta}^{H_\beta}$ and $S_{\omega_b}^{H_\beta}$) need to be evaluated:

$$S_{A_\beta}^{H_\beta} = \frac{\partial H_\beta}{\partial A_\beta}\frac{A_\beta}{H_\beta} = 1 \tag{26}$$

[viii] $U_0 = R_f/R_0\left(V_2-V_1\right)+U_p/2 \Rightarrow U_0 \in \left(0.5\text{ V}\ \ 2.5\text{ V}\right)$ when $I_t \in \left(-3\text{ mA}\ \ 3\text{ mA}\right)$

[ix] f_b=188 Hz

$$S_{\omega_b}^{H_\beta} = \frac{\partial H_\beta}{\partial \omega_b}\frac{\omega_b}{H_\beta} = \frac{\omega^2}{\omega_b^2 + \omega^2}; \ \text{when} \ \omega = 0 \Rightarrow S_{\omega_b}^{H_\beta} = 0$$
$$; \ \text{when} \ \omega = \omega_b \Rightarrow S_{\omega_b}^{H_\beta} = \frac{1}{2} \tag{27}$$

From (26) the sensitivity of the low-frequency gain change can be evaluated, so the A_β depends on the resistances R_f and R_0; if these change by $\pm 1\,\%$ the A_β changes by ± 2, so it follows

$$\frac{\partial H_\beta}{H_\beta} = S_{A_\beta}^{H_\beta}\frac{\partial A_\beta}{A_\beta} = \pm 2\%, \tag{28}$$

Based on (27) the other sensitivities` effects can be evaluated for two cases;

$$\left.\frac{\partial H_\beta}{H_\beta}\right|_{\omega=0} = S_{A_\beta}^{H_\beta}\frac{\partial \omega_b}{\omega_b} = 0 \quad , \tag{29}$$

$$\left.\frac{\partial H_\beta}{H_\beta}\right|_{\omega=\omega_b} = S_{A_\beta}^{H_\beta}\frac{\partial \omega_b}{\omega_b} = -\frac{1}{2}\frac{\partial \omega_b}{\omega_b} \approx 4.7\times 10^{-6}, \tag{30}$$

So, the worst-case precision of the whole analogue part of the *SAMD* is evaluated in (28), and depends only on the precision of the closed-loop gain A_β and, consequently, on the resistances R_f and R_0.

3.1.3 Microcontroller and Communication unit

Digital signal aqcisition device contains the ultra-low-power microcontroller based on the high-performance Arm® Cortex®-M4 32-bit RISC core, operating at a frequency of up to 80 MHz with the possibility of floating-point operation with single precision. It also implements a full set of DSP instructions and a Memory Protection Unit (MPU), which enhances application security. The device offer a fast 12-bit ADC (5 Msps), two comparators, one operational amplifier, two Digital-to-Analogue (DAC) Channels, an internal voltage reference buffer, a low-power RTC etc. The microcontroller unit is capable of operation in a wide temperature range (-40 to +85 °C). The microcontroller could also communicate with the periphery by using TTL gates. This function is exploited for programming the SWD interface. All terminals should be protected against over-voltages.

A quad-band full-featured GSM/GPRS/GNSS module is used for communication unit, using the LCC castellation package with an extensive set of Internet protocols, such as TCP, UDP, PPP, FTP, HTTP, SSL, MQTT, etc. Based on the latest 2G chipset, it has the optimal performance in SMS & data transmission as well as audio service, even in a harsh environment. It features the Dual SIM Single Standby function. The GPRS and GNSS engines are integrated into one compact and low profile SMT package.

A lithium-thionyl chloride battery (Li/SOCl2) was used for the power-supply for all functions This battery type is distinguished by its greater energy density. Due to the low energy consumption of the components, the battery allows autonomous measurements and communication for up to 10 years maintenance free.

4. Experimental Results

For verification of the described measuring principle based on (15) to (18), the experimental test-bench system was built, as shown in Figure 11. The Surge Arrester Monitoring Device has prepared the current measurement results into the form required for further processing. The measurement results are processed with the acquisition units and microcontroller as described in Chapter 3. Then, the results are forwarded to the computer in the “distribution” centre where they are recalculated in order to achieve the right values of the resistive current component.

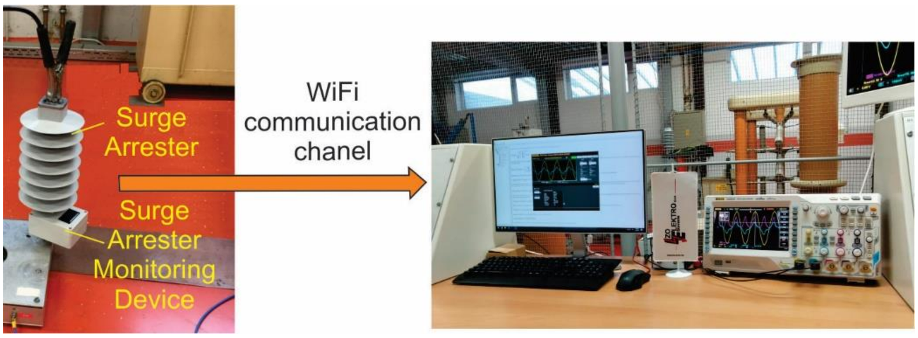

Figure 11: Measurement set-bench

4.1. Experimental test-bench

The proposed algorithm was verified using the test-bench system. For verification purposes the arrester was measured by using the classical oscilloscope measurement (as a reference system), and was also measured by using the proposed described system for extraction of resistive current component $\hat{I}_r$. The surge arrester was connected as indicated in Figure 2 for reference measurement (oscilloscope), and as indicated in Figure 7 for the surge arrester monitoring device. Both measurements were performed at the same operating points.

4.2. Calibration of the Measurement Devices

The signals are provided via the analogue acquistion system to the ADC of the microcontroller. The used ADC allows a voltage between 0 and 3 V on the input terminals. Due to this the single power-supply voltage was also used for safety reasons for the analogue aqcuisition circuit. As a consequency of this, the offset voltage of $U_p/2$ was added to the analogue signal, which represents the leakage current (I_t) information. After the ADC conversion the obtained measuremnet results were sent using the communication unit to the "distribution centre" (computer or server).

4.2.1. Measurement Constant

Figure 12 shows the block scheme of the calibration process. The analogue signal is prepared for ADC conversion in the signal acquisition circuit. The alternative current signal is amplified and shifted by the offset voltage as follows:

$$I_t \in \left(I_{t,\min} \quad I_{t,\max}\right) \Rightarrow \left(V_2 - V_1\right) = U_d \in \left(U_{It,\min} \quad U_{It,\max}\right), \tag{32}$$

$$U_0 = \frac{R_f}{R_0} U_d + Up/2 \Rightarrow U_0 \in \left(U_{0,\min} \quad U_{0,\max}\right), \tag{33}$$

Afterwards, the obtained result is converted to a digital signal using the 12-bit ADC. The offset voltage of 1.5 V corresponds with:

$$U_{0,offset} = U_p / 2 \Rightarrow 2500 = 0000\ 1001\ 1100\ 0100_{binary}, \tag{34}$$

when the $U_{0,\min}$ (0.5 V) is applied on the ADC, input is obtained for:

$$U_{0,\min} = 0.5\ \text{V} \Rightarrow 452 = 0000\ 0011\ 1000\ 0100_{binary}, \tag{35}$$

and when the $U_{0,\max}$ (2.5 V) is applied on the ADC, input is obtained for:

$$U_{0,\max} = 2.5\ \text{V} \Rightarrow 4548 = 0001\ 0001\ 1100\ 0100_{binary}, \tag{36}$$

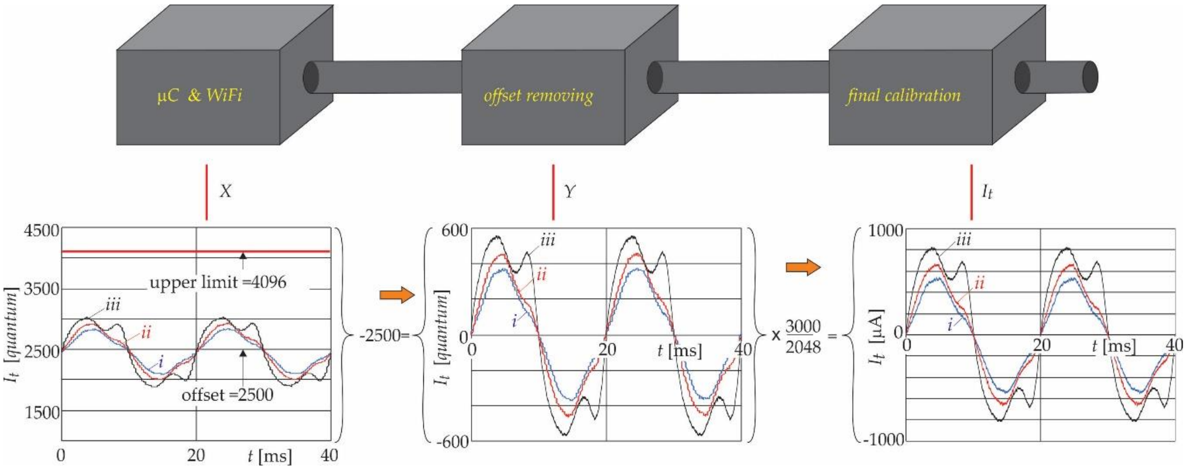

Figure 12: Calibration procedure; roman letters *i*, *ii* and *iii* indicate measurements at 0.80*U*, 1.00*U* and 1.20*U*, respectively.

Due to the 12-bit quantisation the upper voltage is limited to 4096, which means up to the value when the output voltage of the analogue acquisition circuit reaches 2.13 V. Carefully following the above described digitalisation from (24) to (28) it can be concluded that the obtained results, after removing the offset values, should be multiplied by the constant (3000/2048) in order to reconstruct the measured leakage current. So, according to this, and also considering the variables indicated in Figure 12, it follows that;

$$Y = X - 2500 \Rightarrow I_t\left[\mu\text{A}\right] = \frac{I_{t,\max}\left[\mu\text{A}\right]}{4548 - 2500} Y = \frac{3000}{2048} Y = 1.464844\ Y\ , \tag{37}$$

Due to the above mentioned 12-bit quantisation, the input current range should be corrected to:

$$I_t \in \left(I_{t,\min L}\ \ I_{t,\max L}\right) = \left(-2300\ \mu\text{A}\ \ 2300\ \mu\text{A}\right), \tag{38}$$

In practice, the surge arresters are 100% out of order when I_t reaches a magnitude over 1500 μA, so this range guarantees the appropriate consideration of the surge arresters "health" while measuring the resistive component of the leakage current.

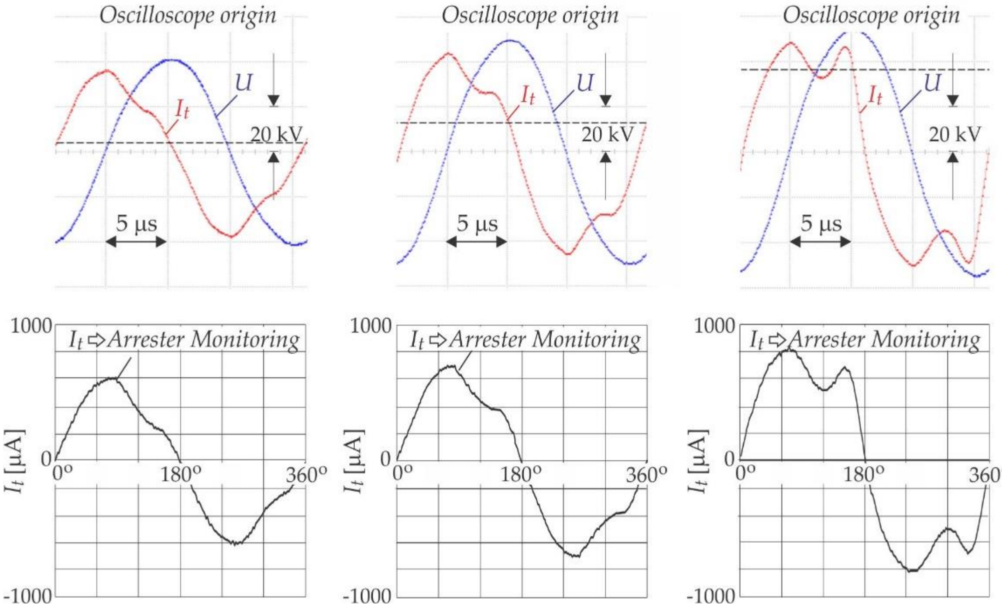

(a) **(b)** **(c)**

Figure 13: Verification of the calibration process when the supply voltages to the surge arrester are: (a) 0.9 *U*; (b) 1.1 *U* and (c) 1.275 *U*.

4.2.2. Verification of the calibration process

The obtained results should be verified in order to justify the measurement principle. Three different operating points of the surge arresters are measured with the oscilloscope and with the Surge Arrester Monitoring Device. Figures 13 (a), (b) and (c) show the results of both measurement principles. The current and voltages waveforms of the surge arrester measured by oscilloscope are shown in the first row.

4.3. Measurement Results

The whole surge arrester monitoring device was tested under laboratory conditions. In order to verify the measurement results, these were compared with the reference resistive current component $\hat{I}_r$ measured by an oscilloscope. From the files obtained from the *SAMD* the leakage current was calibrated appropriately, and the procedure described in chapter 2.3 was applied. The resistive component of leakage current was calculated using (15) to (18). Table 6 summarises the measurement results. The performance indexes (absolute and relative errors) were calculated as follows:

Table 6. Experimental results verification

SAMD Measured I_{t_avg}[μA]	*Calculated* (15)-(18) $\hat{I}_{r\_cal.}$ [μA]	*Reference scope value* $\hat{I}_r$ [μA]	*Absolute error of* $\hat{I}_r$ ε_{abs} [μA]	*Relative error of* $\hat{I}_r$ ε_{rel} [%]
327.3	69.0	79.1	10.1	-12.,8
372.1	103.2	97.0	6.2	6.3
409.7	197.0	195.3	1.7	0.9
411.1	201.1	204.2	-3.1	-1.6
457.0	316.5	311.0	5.5	1.6
581.2	628.5	628.0	0.5	0.1

$$\varepsilon_{abs} = \hat{I}_{r\_cal} - \hat{I}_r\,, \tag{39}$$

and

$$\varepsilon_{rel} = \frac{\hat{I}_{r\_cal} - \hat{I}_r}{\hat{I}_r} \times 100\,, \tag{40}$$

The obtained results have an expected precision, and the measurement principle with the proposed electronic devices can be used for on-line mesurement of the resistive component of surge arrester leakage current.

5. Discussion

Based on the obtained results, it is possible to claim that the measurement principle leads to a so-called "smart" sensor, which enables the measurement of the resistive component of surge arrester leakage current without measuring of the voltage reference. Usually, the surge arrester leakage current and its' resistive component measurement is only performed in a laboratory environment because the method needs the high voltage measurement as well. The proposed method requires that the surge arrester producers should measure the two static characteristics simultaneously. The obtained results were evaluated statistically, and all measurements were in the range of $\left(-2\sigma_{\hat{I}r}, 2\sigma_{\hat{I}r}\right)$. This Standard Deviation parameter can be improved by increasing the number of measured arresters when preparing the two static characteristics of the arrester described in Chapter 2.3. The analogue part of electronic device is designed with a high gain, because the leakage current represents a small quantity compared to the current flowing through the arrester when it is operating due to overvoltage (range of 1000 μA compared with a few kA). Using the described principle, it is possible to design a surge arrester monitoring device and equip every surge arrester mounted in the distribution and transmission grid. The obtained results were promising, and are an excellent guide for design of a reliable, precise and cheap SAMD, appropriate for every installed surge arrester in the high-voltage distribution grid.

Author Contributions

The work presented in the paper was initiated by Vid Vončina from the company Izoelektro d. o. o. Vid Vončina has also performed all the measurements presented here. The basic surge arrester's physics were prepared by Jože Pihler. The analysis of the electronic circuits and necessary software were designed under the guidance of Miro Milanovič. The theoretical analysis was done by Jože Pihler and Miro Milanovič.

Acknowledgments

The authors acknowledge the financial support from the company Izoelektro d. o. o. and the Slovenian Research Agency (Research Core Funding No. P2-0028).

Conflicts of Interest:

The authors declare no conflict of interest.

References

1. Matsuoka, M. Nonohmic Properties of Zinc Oxide Ceramics, *Japanese Journal of Applied Physics*, **1971**, vol. 10, no. 6, pp. 736-746.
2. Levinson, L. M.; Philipp, H. R. The physics of metal oxide varistors, *Journal of Applied Physics*, **1975**, vol. 46, no. 3, pp. 1332–1341.
3. Levine, J. D. Theory of varistor electronic properties, *C R C Critical Reviews in Solid State Sciences*, 1975, vol. 5, no. 4, pp. 597–608.
4. Morris, W. G. Physical properties of the electrical barriers in varistors, *Journal of Vacuum Science and Technology*, **1976**, vol. 13, no. 4, pp. 926–931.
5. Bernasconi, J.; Strässler, S.; Knecht, B.; Klein, H. P.; Menth, A. Zinc oxide based varistors: A possible mechanism, *Solid State Communications*, **1977**, vol. 21, no. 9, pp. 867–870.
6. Emtage, P. R. The physics of zinc oxide varistors, *Journal of Applied Physics*, **1977**, vol. 48, no. 10, pp. 4372–4384.
7. Eda, K. Conduction mechanism of non-Ohmic zinc oxide ceramics, *Journal of Applied Physics*, **1978**, vol. 49, no. 5, pp. 2964–2972.
8. Einzinger, R. Metal oxide varistor action -a homojunction breakdown mechanism, *Applications of Surface Science*, **1978**, vol. 1, no. 3, pp. 329–340.
9. Hower, P. L.; Gupta, T. K. A barrier model for ZnO varistors, *Journal of Applied Physics*, **1979**, vol. 50, no. 7, pp. 4847–4855.
10. Mahan, G. D.; Levinson, L. M.; Philipp, H. R. Theory of conduction in ZnO varistors, *Journal of Applied Physics*, **1979**, vol. 50, no. 4, pp. 2799–2812.
11. Pike, G. E. Diffusion-limited quasi Fermi level near a semiconductor grain boundary, *Physical Review B*, **1984**, vol. 30, no. 6, pp. 3274–3276.
12. Blatter, G.; Greuter, F. Carrier transport through grain boundaries in semiconductors, *Physical Review B*, **1986**, vol. 33, no. 6, pp. 3952–3966.

13. Blatter, G.; Greuter, F. Electrical breakdown at semiconductor grain boundaries, *Physical Review B*, **1986**, vol. 34, no. 12, pp. 8555–8572.
14. Suzuoki, Y.; Muto, H.; Mizutani, T.; and Ieda, M. The role of space charge in the electrical conduction of ethylene-vinyl acetate copolymers, *Journal of Physics D*: Applied Physics, **1987**, vol. 20, no. 8, pp. 1053–1058.
15. Heinrich, C.; Hinrichsen, V. Diagnostics and monitoring of metal-oxide surge arresters in high-voltage networks-comparison of existing and newly developed procedures, *IEEE Transactions on Power Delivery*, **2001**, vol. 16, no. 1, pp. 138–143.
16. Coffeen, L. T.; McBride, J. E. High voltage AC resistive current measurements using a computer based digital watts technique, *IEEE Transactions on Power Delivery*, **1991**, vol. 6, no. 2, pp. 550–556.
17. Metwally, I. A. Performance of distribution-class surge arresters under dry and artificial pollution conditions, *Electrical Engineering*, **2010**, vol. 93, no. 1, pp. 55–62.
18. Shirakawa, S.; Endo, F.; Kitajima, H.; Kobayashi, S.; Goto, K.; Sakai, M. Maintenance of surge arrester by a portable arrester leakage current detector, *IEEE Transactions on Power Delivery*, **1988**, vol. 3, no. 3, pp. 998–1003.
19. Lundquist, J.; Stenstrom, L.; Schei, A.; Hansen, B. New method for measurement of the resistive leakage currents of metal-oxide surge arresters in service, *IEEE Transactions on Power Delivery*, **1990**, vol. 5, no. 4, pp. 1811–1822.
20. Metwally, I. A. Measurement and calculation of surge-arrester residual voltages, *Measurement*, **2011**, vol. 44, no. 10, pp. 1945–1953.
21. Khodsuz, M.; Mirzaie, M.; Harmonics ratios of resistive leakage current as metal oxide surge arresters' diagnostic tools, *Measurement*, **2015**, vol. 70, pp. 148–155.
22. Laurentys Almeida, C. A.; Braga, A. P.; Nascimento, S.; Paiva, V.; Martins, H. J. A.; Torres, R.; Caminhas, W. M. Intelligent Thermographic Diagnostic Applied to Surge Arresters: A New Approach, *IEEE Transactions on Power Delivery*, **2009**, vol. 24, no. 2, pp. 751–757.
23. Lira, G. R. S.; Costa, E. G.; Almeida, C. W. D.; Self-organizing maps applied to monitoring and diagnosis of ZnO surge arresters, **2010** *IEEE/PES Transmission and Distribution Conference and Exposition: Latin America (T&D-LA)*.
24. Neto, E. T. W.; Da Costa, E. G.; Maia, M. Artificial Neural Networks Used for ZnO Arresters Diagnosis, *IEEE Transactions on Power Delivery*, vol. 24, no. 3, pp. 1390–1395, Jul. **2009**, 10.1109/tpwrd.2009.2013402.
25. Wong, K. L. Electromagnetic emission-based monitoring technique for polymer ZnO surge arresters, *IEEE Transactions on Dielectrics and Electrical Insulation*, **2006**, vol. 13, no. 1, pp. 181–190.
26. J. Xu; Z. Ye; L. Luo; A. Kubis; K. Zhou; Electromagnetic field and thermal distribution optimization in shell-type traction transformers, *IET Electric Power Applications*, **2013**, vol. 7, no. 8, pp. 627–632.
27. Zhu, H.; Raghuveer M. R., Influence of Representation Model and Voltage Harmonics on Metal Oxide Surge Arrester Diagnostics, *IEEE Power Engineering Review*, **2001**, vol. 21, no. 8, pp. 62–62.
28. Surge arresters – Part5: Selection and application recommendations IEC 60099-5:2013, **2013**.
29. Electric power transmission and distribution losses (% of output) - World, European Union, Slovenia. Available online: https://data.worldbank.org/indicator/EG.ELC.LOSS.ZS?end=2014&locations=1W-EU-SI&most_recent_value_desc=false&start= **2003** (accessed on 24. 03. 2020).

30. Luo, Y.F. Study on metal-oxide-arrester on-line monitoring distributed- control-system, *M. Eng. Thesis*, School Elect. Eng., Xi'an Jiao tong University, Xi'an, China, **2003**.
31. [EN17] Proizvodnja električne energije po gorivih (kazalec združen v nov kazalec, EN30). Available online: http://kazalci.arso.gov.si/sl/content/proizvodnja-elektricne-energije-po-gorivih-kazalec-zdruzen-v-nov-kazalec-en30?tid= 4 (accessed on 24. 03. **2020**).
32. What is the Carbon inventory? Available online: https://jancovici.com/en/climate-change/ghgs-and-us/what-is-the-carbon-inventory/ (accessed on 24. 03. 2020).